Attributing correlation skill of dynamical GCM precipitation forecasts to statistical ENSO teleconnection using a set theory−based approach

Tongtiegang Zhao[1], Haoling Chen[1], Quanxi Shao[2], Tongbi Tu[1], Yu Tian[3] and Xiaohong Chen[1]

[1] Center of Water Resources and Environment, Southern Marine Science and Engineering Guangdong Laboratory (Zhuhai), School of Civil Engineering, Sun Yat-Sen University, Guangzhou, China
[2] CSIRO Data61, Australian Resources Research Centre, Bentley, WA, Australia
[3] Department of Water Resources, China Institute of Water Resources and Hydropower Research, Beijing, China

Abstract. Climate teleconnections are essential for the verification of valuable precipitation forecasts generated by global climate models (GCMs). This paper develops a novel approach to attributing correlation skill of dynamical GCM forecasts to statistical El Niño-Southern Oscillation (ENSO) teleconnection by using the coefficient of determination (R^2). Specifically, observed precipitation is respectively regressed against GCM forecasts, Niño3.4 and both of them and then the intersection operation is implemented to quantify the overlapping R^2 for GCM forecasts and Niño3.4. The significance of overlapping R^2 and the sign of ENSO teleconnection facilitate three cases of attribution, i.e., significantly positive anomaly correlation attributable to positive ENSO teleconnection, attributable to negative ENSO teleconnection and not attributable to ENSO teleconnection. A case study is devised for the Climate Forecast System version 2 (CFSv2) seasonal forecasts of global precipitation. For grid cells around the world, the ratio of significantly positive anomaly correlation attributable to positive (negative) ENSO teleconnection is respectively 10.8% (11.7%) in December-January-February (DJF), 7.1% (7.3%) in March-April-May (MAM), 6.3% (7.4%) in June-July-August (JJA) and 7.0% (14.3%) in September-October-November (SON). The results not only confirm the prominent contributions of ENSO teleconnection to GCM forecasts, but also present spatial plots of regions where significantly positive anomaly correlation is subject to positive ENSO teleconnection, negative ENSO teleconnection and teleconnections other than ENSO. Overall, the proposed attribution approach can serve as an effective tool to investigate the sources of predictability for GCM seasonal forecasts of global precipitation.

1 Introduction

Precipitation is one of the most important hydrological variables and is an integral part of the global water cycle (Scofield & Kuligowski, 2003; Huffman et al., 2007; Ushio et al., 2009; Schneider et al., 2016; Beck et al., 2019). It plays a key role in driving hydrological processes at catchment, regional and continental scales (e.g., Robertson et al., 2013; Wu et al., 2014; Yuan et al., 2014; Greuell et al., 2018; Lakshmi & Satyanarayana, 2019). Despite the importance, the forecasting of precipitation remains a formidable task due to complex interactions of ocean, atmosphere and land surface processes (Doblas-Reyes et al., 2013; Vano et al., 2014; Johnson et al., 2019; Zhao et al., 2019; Tesfa et al., 2020). Comparing multiple sets of

global temperature and precipitation forecasts from the North American Multi-Model Ensemble (NMME) experiment, Becker et al. (2020) highlighted that there are substantial improvements in temperature forecasts over both land and ocean during the past decades and that there is still plenty of room for improvement of global precipitation forecasts.

35 Global climate models (GCMs) generate valuable forecasts of worldwide precipitation for hydrological modelling and water management (Doblas-Reyes et al., 2013; Kirtman et al., 2014; Schepen et al., 2020). Nowadays, GCMs have been employed by major climate centers around the world to produce operational climate outlooks (Demargne et al., 2014; Delworth et al., 2020). For example, the Climate Forecast System version 2 (CFSv2) of the U.S. National Centers for Environmental Prediction (NCEP) has been implemented for coupled ocean-atmosphere forecasting since 2011 (Saha et al., 2010); the European Centre

40 for Medium-Range Weather Forecasts (ECMWF) System 5 model became operational in 2017 (Johnson et al., 2019); and the Seamless System for Prediction and Earth System Research (SPEAR) became the next generation modelling system at the Geophysical Fluid Dynamics Laboratory (GFDL) in 2020 (Delworth et al., 2020). In the meantime, GCM forecasts have been increasingly incorporated into forecasting systems of streamflow, crop yield and soil water and they are shown to create enormous socioeconomic benefits (e.g., Vano et al., 2014; Peng et al., 2018; Wang et al., 2019).

45 Climate teleconnections, which are widely used in conventional statistical hydrological forecasting (Lima & Lall, 2010; Steinschneider & Lall, 2016; Mendoza et al., 2017; Mortensen et al., 2018; Wang et al., 2020), are an essential part in assessing the skill of GCM forecasts (Neelin & Langenbrunner, 2013). That is, a number of teleconnection patterns are usually investigated upon the issuance of a new set of GCM forecasts (Kim et al., 2012; Jia et al., 2015; Delworth et al., 2020). For example, El Niño-Southern Oscillation (ENSO) and Madden-Julian oscillation (MJO) have been investigated for CFSv2

50 forecasts (Saha et al., 2014). North Atlantic Oscillation (NAO), Arctic Oscillation (AO) and Pacific North American (PNA) teleconnections have been assessed for Global Earth Observing System (GEOS) modeling and data assimilation system (Molod et al., 2020). ENSO and Pacific decadal oscillation (PDO) have been examined for GFDL-SPEAR forecasts (Delworth et al., 2020). It is generally found that skilful GCM forecasts are owing to effective formulations of teleconnection patterns (e.g., Molteni et al., 2011; Merryfield et al., 2013; Saha et al., 2014; Jia et al., 2015; Delworth et al., 2020).

55 There have been in-depth investigations of ENSO for GCM forecasts as it is one of the most prominent modes of climate variability (Fu et al., 1997; Wang et al., 2003; Feng & Hao, 2021). For example, the influence of ENSO on the East Asian-western Pacific climate was studied for CFSv2 forecasts (Yang & Jiang, 2014) and also for climate projections in the Coupled Model Inter-comparison Project Phase 5 (Gong et al., 2015; Kim et al., 2016; Kim & Kug, 2018). The relationship between forecast skill and the state of sea surface temperatures (SSTs) was evaluated for the seasonal outlook of precipitation over the

60 United States and the skill was found to be dominantly attributed to ENSO in late autumn to late spring (Quan et al., 2006; Pegion & Kumar, 2013; Shin et al., 2019). Understanding the sources for predictability is important for physically-based validations of GCM forecasts (Neelin & Langenbrunner, 2013; Manzanas et al., 2014; Shin et al., 2019). Nevertheless, previous studies tended to pay attention to regions subject to prominent ENSO influences (Kim et al., 2016; Rivera & Arnould, 2020; Vashisht et al., 2021). At the global scale, the attribution of GCM precipitation forecasts to ENSO teleconnection is yet to be

65 conducted.

This paper is devoted to attributing correlation skill of dynamical CFSv2 forecasts (e.g., Saha et al., 2010; Yuan et al., 2011; Jia et al., 2015; Becker et al., 2020; Zhao et al., 2020a) to statistical ENSO teleconnection at the global scale. A novel approach based on the set theory is devised to facilitate the attribution. With the coefficient of determination (R^2) characterizing the ratio of explained variance and the set operations illustrating the overlapping R^2, the significance test by grid cell is conducted by bootstrapping in order to identify where correlation skill is attributable to ENSO teleconnection. As will be demonstrated through the case study of CFSv2 forecasts, three cases are effectively revealed: (1) significantly positive anomaly correlation attributable to positive ENSO teleconnection, (2) significantly positive anomaly correlation attributable to negative ENSO teleconnection and (3) significantly positive anomaly correlation not attributable to ENSO teleconnection.

2 Data description

GCM forecasts comprise a typical high-dimensional dataset (Kirtman et al., 2014; Saha et al., 2014; Chen & Kumar, 2016; Becker et al., 2020; Zhao et al., 2020b). For the CFSv2 forecasts investigated in this paper, there are five dimensions: (1) forecast start time s; (2) lead time l; (3) ensemble size n; (4) latitude y; and (5) longitude x. s represents the number of months since the benchmark time that is January 1982; l is the number of months ahead, which ranges from 0 to 9 month for the CFSv2 forecasts; $n = 1, \ldots, 24$, i.e., the total number of ensemble members is 24; y ranges from -90 to 90 while x is from 0 to 359, with a horizontal resolution of 1.0° latitude by 1.0° longitude. The set of forecasts is denoted by

$$F = \left[f_{s,l,n,y,x} \right], \tag{1}$$

in which f represents forecast values specified by the five dimensions and F is the dataset of forecasts.

There are three dimensions for the dataset of observed precipitation corresponding to forecasts (Xie et al., 2007; Infanti & Kirtman, 2015; Schneider et al., 2016). They are target time t, which is equal to the sum of start time s and lead time l to align observations with forecasts; latitude y; and longitude x. The set of observed precipitation corresponding to the forecasts is denoted as

$$O = \left[o_{t,y,x} \right] \quad (t = s + l). \tag{2}$$

The CPC global daily Unified Rain-gauge Database (CPC-URD), which has been widely used in the analysis of regional and global precipitation (Xie et al., 2010), is used as the referenced observed precipitation.

The correlation skill, which is in the form of the Pearson's correlation coefficient, is calculated so as to relate CFSv2 precipitation forecasts to CPC-URD observations:

$$r(o, f) = \frac{\sum_k (o_k - \bar{o})(f_k - \bar{f})}{\sqrt{\sum_k (o_k - \bar{o})^2} \sqrt{\sum_k (f_k - \bar{f})^2}}. \tag{3}$$

In Eq. (3), k represents the target year (k=1982, 1983, …, 2010), where other dimensions of o and f are omitted for the sake of simplicity. The value of $r(o, f)$ measures how well CFSv2 forecasts correspond to observed precipitation. A significantly positive $r(o, f)$ implies that large (small) forecasts are indicative of large (small) observations, whereas a neutral or negative $r(o, f)$ indicates non-skilful forecasts (Yuan et al., 2011; Zhao et al., 2020a; Zhao et al., 2020b).

It is noted that forecasts/observations, which are monthly, are aggregated into seasonal. The aggregation is meant to facilitate the analysis by season. The attention is paid to the latest forecasts. That is, seasonal precipitation forecasts generated at the beginning of the season are investigated. For example, the December-January-February (DJF) forecasts are generated at the beginning of December. Similarly, seasonal forecasts for March-April-May (MAM), June-July-August (JJA) and September-October-November (SON)) are respectively produced at the starts of March, June and September.

The concurrent correlation between Niño3.4 and CPC-URD observations is employed to represent ENSO teleconnection (Cai et al., 2009; Kim & Kug, 2018; Steptoe et al., 2018):

$$r(o, \tilde{\text{Niño3.4}}) = \frac{\sum_k (o_k - \bar{o})(\tilde{\text{Niño3.4}}_k - \overline{\tilde{\text{Niño3.4}}})}{\sqrt{\sum_k (o_k - \bar{o})^2} \sqrt{\sum_k (\tilde{\text{Niño3.4}}_k - \overline{\tilde{\text{Niño3.4}}})^2}} . \tag{4}$$

Niño3.4 is a commonly used index of ENSO (Mason & Goddard, 2001; Chen & Kumar, 2020; Vashisht et al., 2021). The sign of $r(o, \text{Niño3.4})$ indicates the effects of ENSO. A positive $r(o, \text{Niño3.4})$ means that high (low) values of Niño3.4 correspond to large (small) values of observed precipitation, i.e., El Niño events associate with wet conditions whereas La Niña events relate to dry conditions. By contrast, a negative $r(o, \text{Niño3.4})$ indicates that high (low) values of Niño3.4 coincide with below-normal (above-normal) precipitation.

3 Methods

3.1 Mathematical formulation

The approach to attributing correlation skill of GCM seasonal forecasts to ENSO teleconnection is built upon the coefficient of determination, i.e., R^2 (Koster et al., 2010). Mathematically, R^2 is equivalent to the squared value of the Pearson's correlation coefficient r (Krause et al., 2005)

$$R^2(Y \sim X) = r^2(Y, X). \tag{5}$$

There is a difference in the meaning of r in relating observed precipitation to forecasts and ENSO. As to forecasts, r tends to be positive, i.e., high (low) values of forecasts can be indicative of high (low) values of observations (Yuan et al., 2011; Zhao et al., 2020a; Zhao et al., 2020b). However, ENSO teleconnection can be either positive or negative. For example, in DJF, positive $r(o, \text{Niño3.4})$ tends to be dominant over southern North America and negative $r(o, \text{Niño3.4})$ are generally prevalent over northern South America (Mason & Goddard, 2001).

Both positive and negative correlations contribute to R^2. R^2 is respectively derived for forecasts and ENSO in relating them to observed precipitation. Specifically, simple linear regression models are set up to regress observed precipitation respectively against GCM forecasts and Niño3.4:

$$o_k = \alpha_1 + \beta_1 f_k + \epsilon_{1,k} \Rightarrow R^2(o \sim f) = 1 - \frac{\sum_k \epsilon_{1,k}^2}{\sum_k (o_k - \bar{o})^2} \ , \tag{6}$$

$$o_k = \alpha_2 + \beta_2 \tilde{\text{Niño3.4}}_k + \epsilon_{2,k} \Rightarrow R^2(o \sim \text{Niño3.4}) = 1 - \frac{\sum_k \epsilon_{2,k}^2}{\sum_k (o_k - \bar{o})^2} \ , \tag{7}$$

where β_1 and β_2 are the regression coefficients; ϵ_1 and ϵ_2 are the residuals; k represents the target year. Further, through bi-variate linear regression, the variance explained by the union of forecasts and Niño3.4 is calculated:

$$o_k = \alpha_3 + \beta_{3,1} f_k + \beta_{3,2} \tilde{\text{Niño3.4}}_k + \epsilon_{3,k} \Rightarrow R^2(o \sim f \cup \text{Niño3.4}) = 1 - \frac{\sum_k \epsilon_{3,k}^2}{\sum_k (o_k - \bar{o})^2} \ , \tag{8}$$

in which the union operator is introduced to represent the joint effect. If GCM forecasts were independent from Niño3.4, then $R^2(o \sim f \cup \text{Niño3.4})$ could conceptually be obtained by simply adding up $R^2(o \sim f)$ and $R^2(o \sim \text{Niño3.4})$. On the other hand, if GCM forecasts were dependent on Niño3.4, then there would be some overlaps for $R^2(o \sim f)$ and $R^2(o \sim \text{Niño3.4})$. As a result, $R^2(o \sim f \cup \text{Niño3.4})$ would not be as large as the sum of $R^2(o \sim f)$ and $R^2(o \sim \text{Niño3.4})$.

According to the set theory, the intersection between $R^2(o \sim f)$ and $R^2(o \sim \text{Niño3.4})$ is derived by subtracting $R^2(o \sim f \cup \text{Niño3.4})$ from the sum of $R^2(o \sim f)$ and $R^2(o \sim \text{Niño3.4})$:

$$\begin{aligned} R^2(o \sim f \cap \text{Niño3.4}) = R^2(o \sim f) + R^2(o \sim \text{Niño3.4}) \\ - R^2(o \sim f \cup \text{Niño3.4}) \end{aligned} \ , \tag{9}$$

in which the intersection operator is introduced to formulate the overlapping R^2 between forecasts and Niño3.4. Specifically, the value of $R^2(o \sim f \cap \text{Niño3.4})$ quantifies the overlapping part of the explained variance of observed precipitation accounted for by both GCM forecasts and Niño3.4.

3.2 Attribution of correlation skill

There are three steps to attribute correlation skill of GCM forecasts to ENSO teleconnection. As shown in Figure 1, the first step is the implementation of three linear regression models to derive $R^2(o \sim f)$, $R^2(o \sim \text{Niño3.4})$ and $R^2(o \sim f \cup \text{Niño3.4})$ so as to derive $R^2(o \sim f \cap \text{Niño3.4})$. In the absence of a theoretical distribution function for the overlapping R^2, the significance is tested by randomly permuting GCM forecasts and Niño3.4 for 1000 times under the null hypothesis that observed precipitation was independent from either GCM forecasts or Niño3.4. In this way, $R^2(o \sim f \cap \text{Niño3.4})$ is tested to examine whether the overlapping R^2 between f and Niño3.4 is significant.
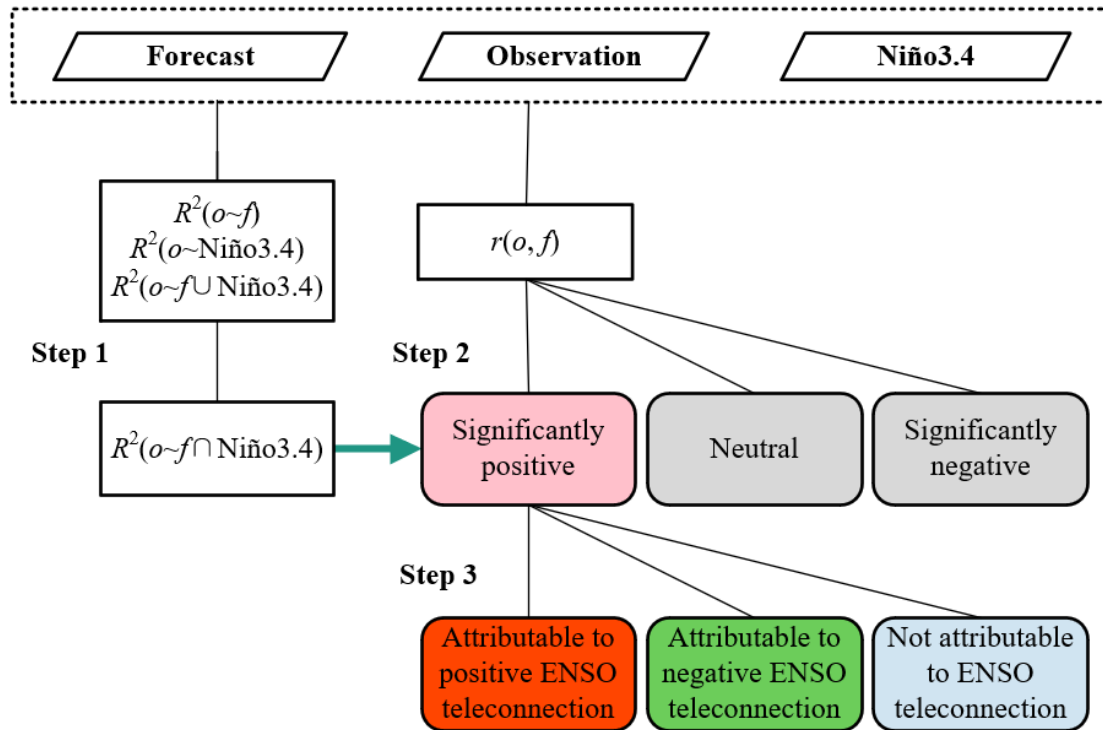
Figure 1: Flowchart of the three steps that attribute significantly positive anomaly correlation of GCM forecasts to ENSO teleconnection.

Secondly, the significance of correlation coefficient is calculated for GCM forecasts in relating them to global precipitation. Specifically, $r(o, f)$ is obtained for each grid cell over global land. The two-tailed significance test is implemented and $r(o, f)$ is therefore identified to be significantly positive, neutral or significantly negative. In this paper, the significance levels in the first and second steps are set to be 0.10.

The third step focuses on significantly positive $r(o, f)$ that indicates informative forecasts (Becker et al., 2020; Zhao et al., 2020a; Zhao et al., 2020b). There are two criteria: (1) the significance of overlapping R^2 and (2) the sign of ENSO teleconnection. Overall, three cases are obtained: (1) significantly positive anomaly correlation attributable to positive ENSO teleconnection, (2) significantly positive anomaly correlation attributable to negative ENSO teleconnection and (3) significantly positive anomaly correlation not attributable to ENSO teleconnection.

3.3 An illustrative example

An example based on synthetic data is devised to illustrate how the overlapping R^2 for the response variable y is influenced by the association between two explanatory variables x_1 and x_2. Samples of x_1, x_2 and y are randomly drawn from a tri-variate normal distribution

$$[x_1, x_2, y]^{\mathrm{T}} \sim N(\mathbf{\mu}, \mathbf{\Sigma}),\qquad(10)$$

155 where $\mathbf{\mu}$ and $\mathbf{\Sigma}$ are the mean vector and covariance matrix, respectively:

$$\mathbf{\mu}^{\mathrm{T}} = [0,0,0],\qquad(11)$$

$$\mathbf{\Sigma} = \begin{bmatrix} 1 & r(x_1, x_2) & 0.5 \\ r(x_1, x_2) & 1 & 0.5 \\ 0.5 & 0.5 & 1 \end{bmatrix}.\qquad(12)$$

In the example, the correlations of y with x_1, x_2 are fixed to be 0.5 respectively. As a result, the focus is on $r(x_1, x_2)$ that determines the intersection between x_1 and x_2. The value of $r(x_1, x_2)$ is set to be 0.0, 0.1, 0.2, 0.3, 0.4 and 0.5. For each pre-specified $r(x_1, x_2)$, 1000 samples of x_1, x_2 and y are drawn to facilitate linear regression models to derive $R^2(y{\sim}x_1)$, $R^2(y{\sim}x_2)$, $R^2(y{\sim}x_1 \cup x_2)$ and $R^2(y{\sim}x_1 \cap x_2)$. For R^2, the median and inter-quartile ranges are estimated through 1000 Monte Carlo

160 experiments.
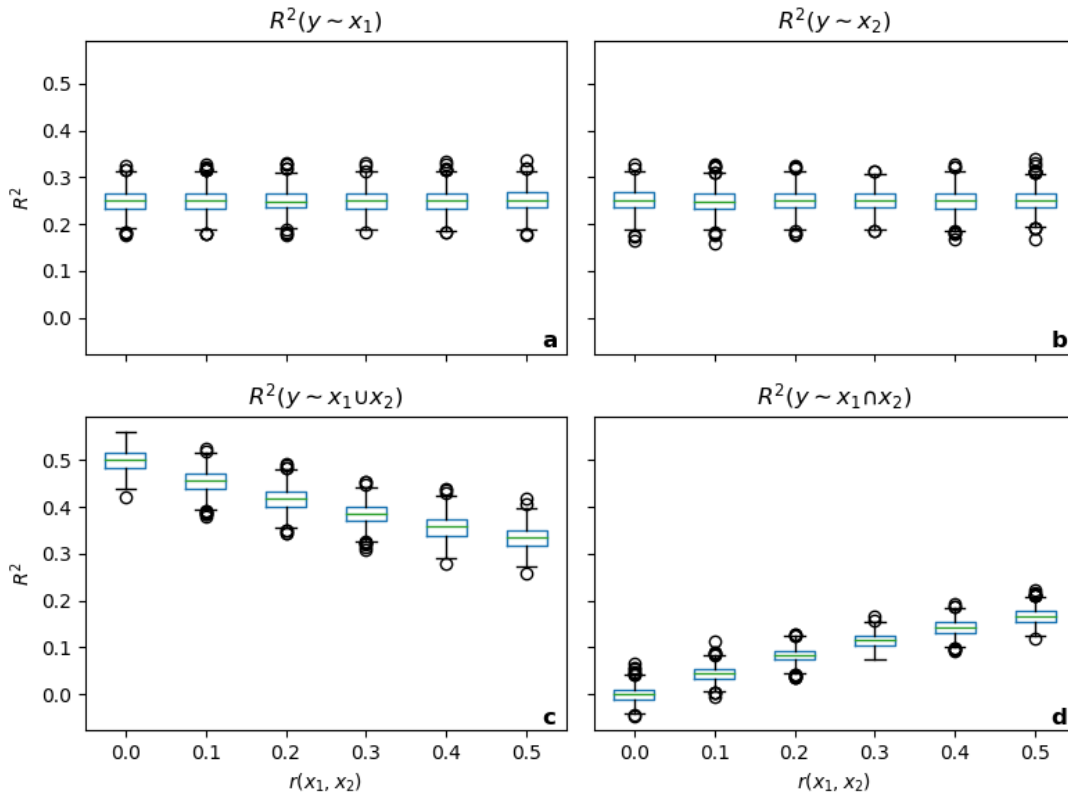
Figure 2: Boxplots of coefficient of determination (R^2) for (a) $R^2(y\sim x_1)$, (b) $R^2(y\sim x_2)$, (c) $R^2(y\sim x_1 \cup x_2)$ and (d) $R^2(y\sim x_1 \cap x_2)$ in the Monte Carlo experiments.

165

Figures 2 illustrates the influences of $r(x_1, x_2)$ on $R^2(y\sim x_1)$, $R^2(y\sim x_2)$, $R^2(y\sim x_1 \cup x_2)$ and $R^2(y\sim x_1 \cap x_2)$. Figures 2a and 2b show that the median values of $R^2(y\sim x_1)$ and $R^2(y\sim x_2)$ approximate the squared value of pre-specified $r(y, x_1)$ and $r(y, x_2)$. That is, they remain to be around 0.25, i.e., 0.5^2, as $r(x_1, x_2)$ increases from 0.0 to 0.5. The indication is that the change in correlation between forecasts and Niño3.4 does not influence the amount of information that they respectively provide for observed

170   precipitation. By contrast, Figure 2c shows that $R^2(y\sim x_1 \cup x_2)$, which represents the ratio of variance explained by the union of x_1 and x_2, decreases with the increase of $r(x_1, x_2)$. This phenomenon coincides with the increase of $R^2(y\sim x_1 \cap x_2)$ with $r(x_1, x_2)$.
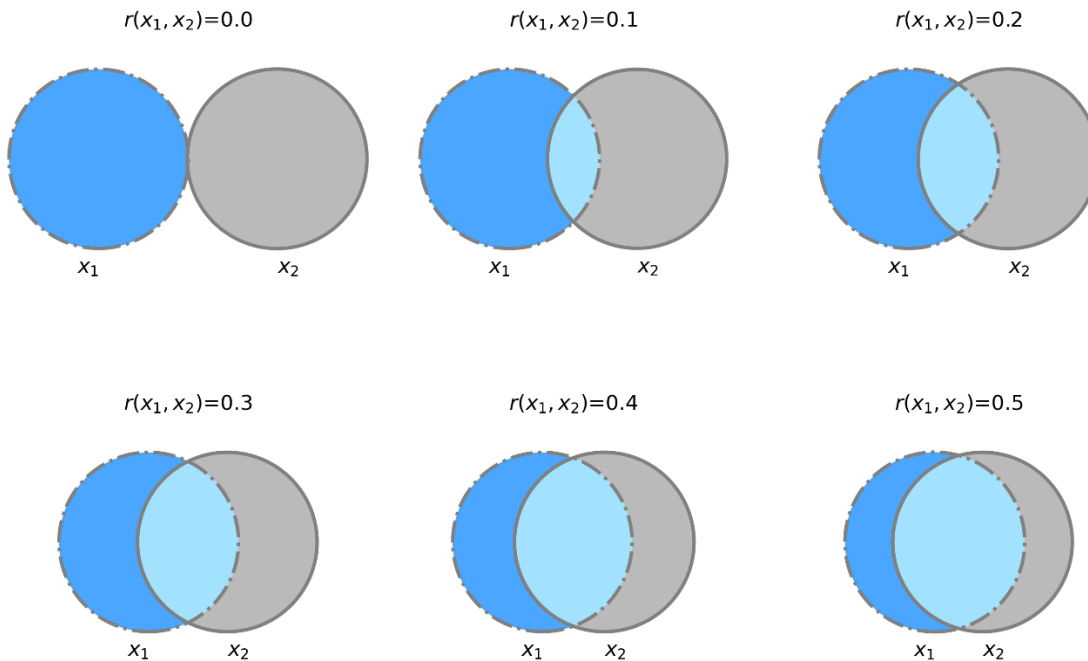
Figure 3: Venn diagrams for the variance of y explained by x_1 and x_2 given six levels of correlation between x_1 and x_2.

175

Figure 3 further shows the influence of $r(x_1, x_2)$ by using the Venn diagram that illustrates the extent to which $R^2(y\sim x_1)$ and $R^2(y\sim x_2)$ intersect. The intersection is represented by the overlapping area between the two circles. From this figure, it can be seen that it is the correlation between x_1 and x_2 that leads to the decrease of $R^2(y\sim x_1 \cup x_2)$ and the increase of $R^2(y\sim x_1 \cap x_2)$. For global precipitation forecasting, the intersection reflects the overlapping R^2 for GCM forecasts and ENSO teleconnection.

180   Figure 3 indicates that the correlation between GCM forecasts and Niño3.4 would lead to a decrease of total information and an increase of overlapping information.

4 Results

4.1 Correlation skill and ENSO teleconnection in DJF

Global maps of correlation skill and ENSO teleconnection in DJF, which is the peak season of ENSO, are shown in the upper part of Figure 4. In Figure 4a, correlation skill is observed to be largely positive, indicating that CFSv2 forecasts are skilful in general (Saha et al., 2010). In Figure 4b, ENSO teleconnection exhibits both positive and negative values. That is, observed precipitation around the world can be positively or negatively correlated with Niño3.4 (Mason & Goddard, 2001; Chen & Kumar, 2020; Vashisht et al., 2021). The two-tailed significance test is applied to anomaly correlation and ENSO teleconnection at each grid cell. Figure 4c illustrates that correlation skills of CFSv2 forecasts are significantly positive over extensive areas around the globe. Moreover, Figure 4c is observed to correspond to Figure 4d to some extent – significantly positive correlations appear over southern North America and East Africa in both Figures 4c and 4d. In addition, significantly positive anomaly correlation (Figure 4c) correspond to significantly negative ENSO teleconnections (Figure 4d) in northern South America, southern Africa and Southeast Asia.

The results of simple linear regressions that lay the foundation for the attribution analysis are shown in Figures 4e to 4h. Figures 4e and 4f, which are respectively for CFSv2 forecasts and Niño3.4, respectively conform to Figures 4a and 4b. This outcome is due to that R^2 is mathematically equal to the squared value of correlation coefficient (Krause et al., 2005). The union in Figure 4g exhibits a higher value of R^2 than that in either Figure 4e or Figure 4f. The subtraction of the union from the sum facilitates the intersection. As illustrated in Figure 4h, deep blue grid cells are seen to distribute in southern North America, northern South America, East Africa, Southern Africa and Southeast Asia. Over these regions, both GCM forecasts and Niño3.4 index can explain a considerable ratio of the variance of observed precipitation (Figures 4e and 4f). More importantly, their explained variances intersect (Figure 4h).
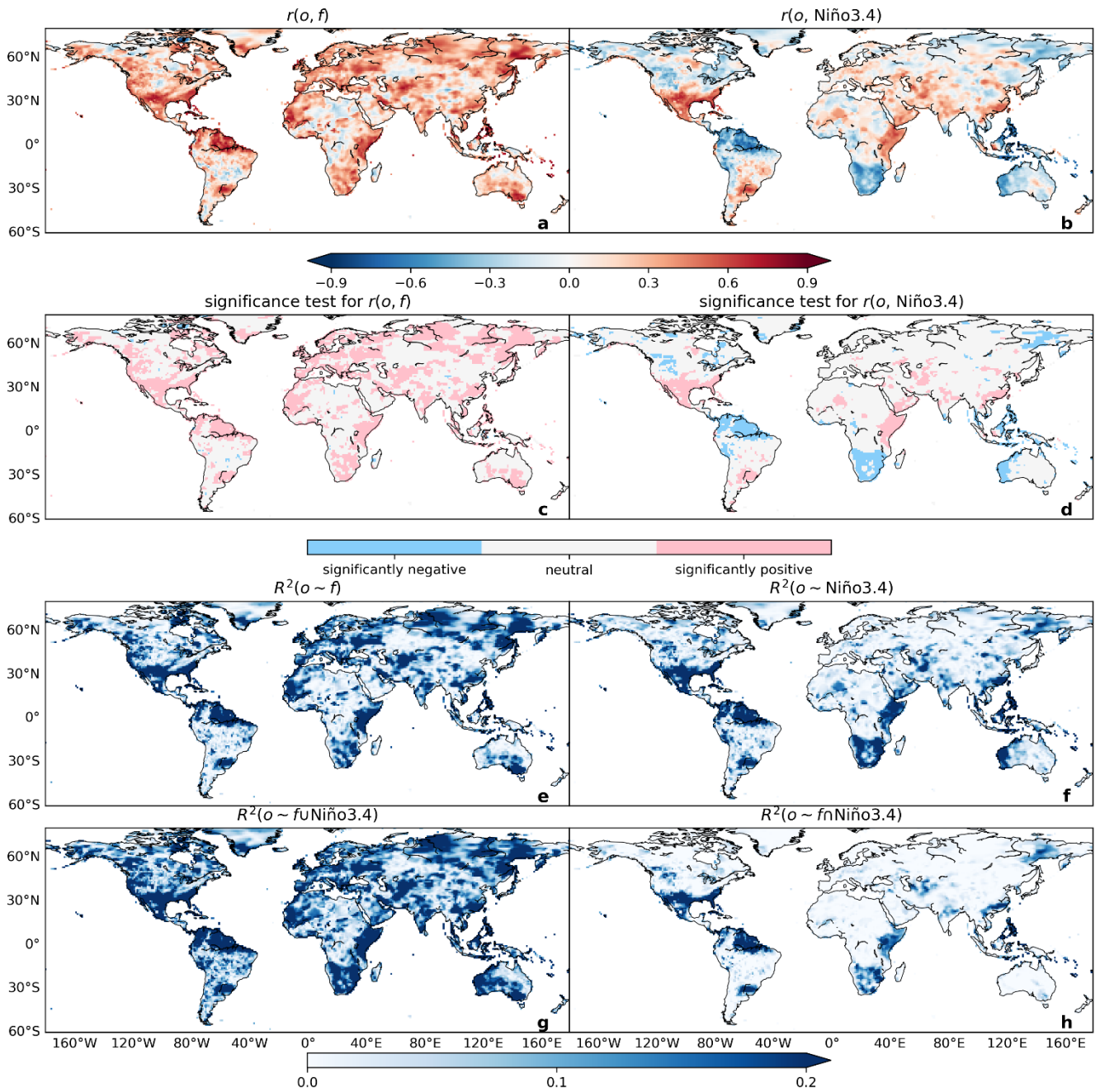
Figure 4: Correlation coefficients between observed precipitation in DJF with (a) 0-month lead CFSv2 forecasts generated at the beginning of December and (b) concurrent Niño3.4. Significance tests of correlation for (c) CFSv2 forecasts and (d) Niño3.4. Coefficient of determination (R^2) for the regression of observed precipitation against (e) CFSv2 forecasts; (f) Niño3.4; (g) the union of CFSv2 forecasts and Niño3.4 and (h) the intersection of CFSv2 forecasts and Niño3.4.

4.2 Attribution at the global scale

The significance of the overlapping R^2 for CFSv2 forecasts and Niño3.4 is shown in Figure 5. In Figure 5a, grid cells with significant overlapping R^2 are marked in orange. The corresponding anomaly correlation and ENSO teleconnection, which are respectively obtained from Figure 4a and Figure 4b, are illustrated using scatter plot in Figure 5b. The scatter points tend fall towards the upper right and left corners of the plot. The implication is that both anomaly correlation and ENSO teleconnection ought to be large enough to facilitate a significant intersection. Largely owing to overlapping R^2, anomaly correlation is observed to increase with the increase of positive ENSO teleconnection and also with the decrease of negative ENSO teleconnection. For Figure 5b, there notably exist some outliers that suggest ENSO teleconnection could contribute to negative anomaly correlation. CFSv2 forecasts are generally wrong in these cases and the cautious grid cells are marked in black in Figure 5a. Further, the scatter plot in Figure 5c is for grid cells where overlapping R^2 is non-significant. For a fair number of grid cells, anomaly correlation can rise above 0.50 but ENSO teleconnection remains nearly 0.00. The implication is that the corresponding anomaly correlation is not relevant to ENSO teleconnection.
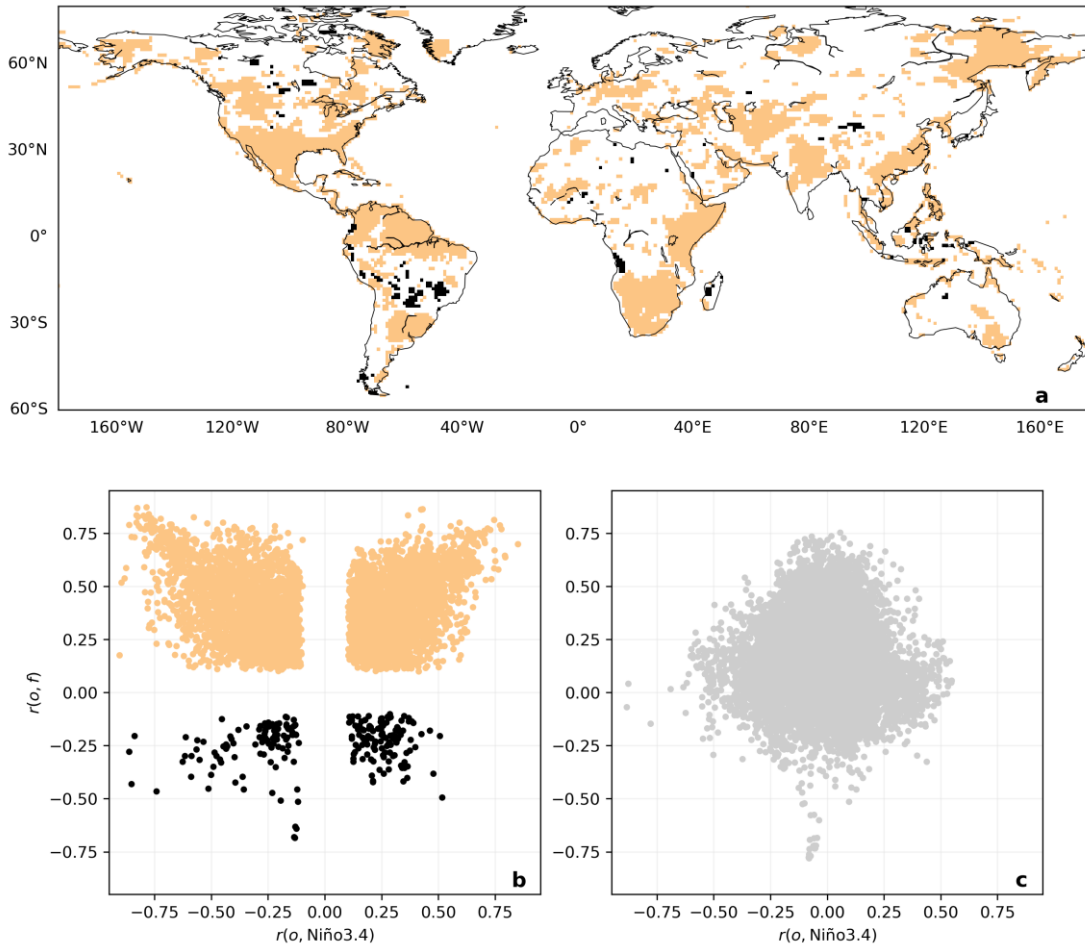
Figure 5: (a) Spatial distribution of grid cells with significant overlapping R^2 for CFSv2 forecasts generated in December and Niño3.4 in DJF. Scatter plots of anomaly correlation against ENSO teleconnection for grid cells (b) with significant overlapping R^2 and (c) with non-significant overlapping R^2. Grey points in subplot (c) are marked in white in subplot (a).

Figure 6 presents the three cases of attribution of significantly positive anomaly correlation. The red colour marks grid cells where significantly positive anomaly correlation is attributable to positive ENSO teleconnection. Some corresponding grid cells are observed in regions of known positive ENSO teleconnections, such as southern North America (Strazzo et al., 2019) and equatorial eastern Africa (Vashisht et al., 2021); and some are in less-investigated regions, such as parts of Central, South and East Asia. The green colour indicates grid cells where significantly positive anomaly correlation is attributable to negative ENSO teleconnection. They appear in northern South America and southern Africa, where negative ENSO teleconnection is known to exist (Howard et al., 2019; Cai et al., 2020) and also in parts of Far East and Alaska. There are also grey areas where significantly positive anomaly correlation is not attributable to ENSO teleconnection. The corresponding grid cells are

235 generally located in Europe, North Asia, northwestern Africa and South Australia. Therein, skilful forecasts can relate to teleconnections other than ENSO, such as AO and NAO (Minami & Takaya, 2020).
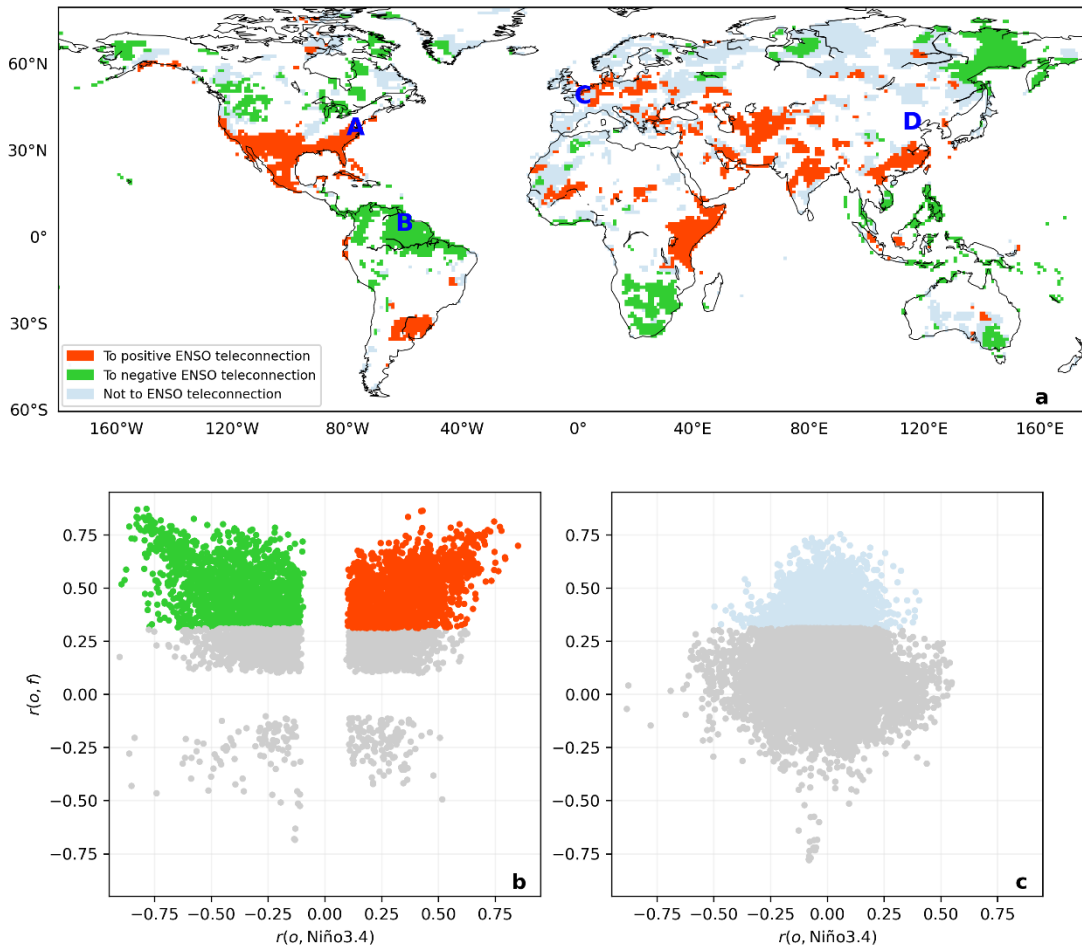
Figure 6: (a) Spatial distribution of grid cells for the three cases attributing anomaly correlation of CFSv2 forecasts to ENSO
240 teleconnection. Scatter plots of anomaly correlation against ENSO teleconnection for grid cells (b) with significant overlapping R^2 and (c) without significant overlapping R^2. Grey points in subplots (b) and (c) are marked in white in subplot (a). Four grid cells are selected and labelled by capital letters from subplot (a) for the subsequent analysis of the attribution of CFSv2 forecasts to ENSO teleconnection.

245 Figure 7 presents a sunburst diagram that quantifies the percentages of significantly positive anomaly correlation and its attribution results. As shown by the central cycle, anomaly correlation is identified to be significantly positive, neutral, or significantly negative (Zhao et al., 2020a; Zhao et al., 2020b). The grey slice suggests that more than half of grid cells around the globe are of neutral anomaly correlation, indicating that GCM precipitation forecasts still have plenty of room for improvement (Kim et al., 2012; Jia et al., 2015; Delworth et al., 2020). The pink slice indicates that 39.4% of the grid cells

250 exhibit significantly positive anomaly correlation. There exist three cases of attribution for significantly positive anomaly correlation. The results are shown by the extended slices, of which the colour scheme is the same as that of Figure 6. It can be seen that significantly positive anomaly correlation is attributable to positive (negative) teleconnections for 10.8% (11.7%) of grid cells around the globe. Further, significantly positive anomaly correlation is not attributable to ENSO teleconnection for 16.9% of grid cells around the globe.

255
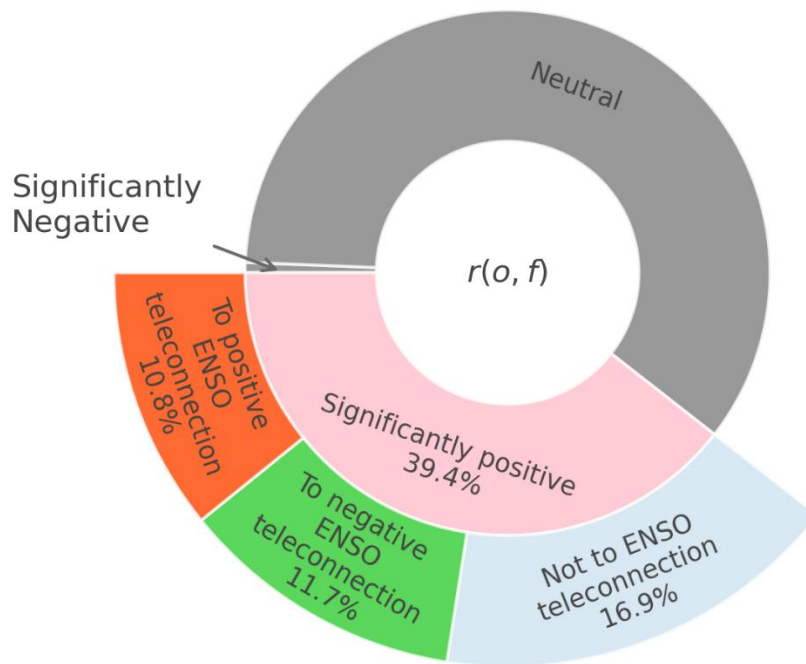
Figure 7: Sunburst diagram of the attribution of significantly positive anomaly correlation to ENSO teleconnection for CFSv2 forecasts in DJF.

260 4.3 Attribution for selected grid cells

Four grid cells are selected from Figure 6a to showcase the attribution of CFSv2 forecasts to ENSO teleconnection. As is illustrated in the section of methods, there are three variables under investigation. They are observed precipitation, forecast precipitation and Niño3.4. Their values are normalized, i.e., subtracting the mean and dividing by the standard deviation, to facilitate the inter-comparison of results across the four grid cells. In Figure 8, the first column plots normalized observation

265   against normalized forecasts; the second column plots normalized observation against normalized Niño3.4; and the third

column plots normalized forecasts against normalized Niño3.4. Furthermore, the last column of Figure 8 presents the Venn

diagrams illustrating the set operation of intersection.
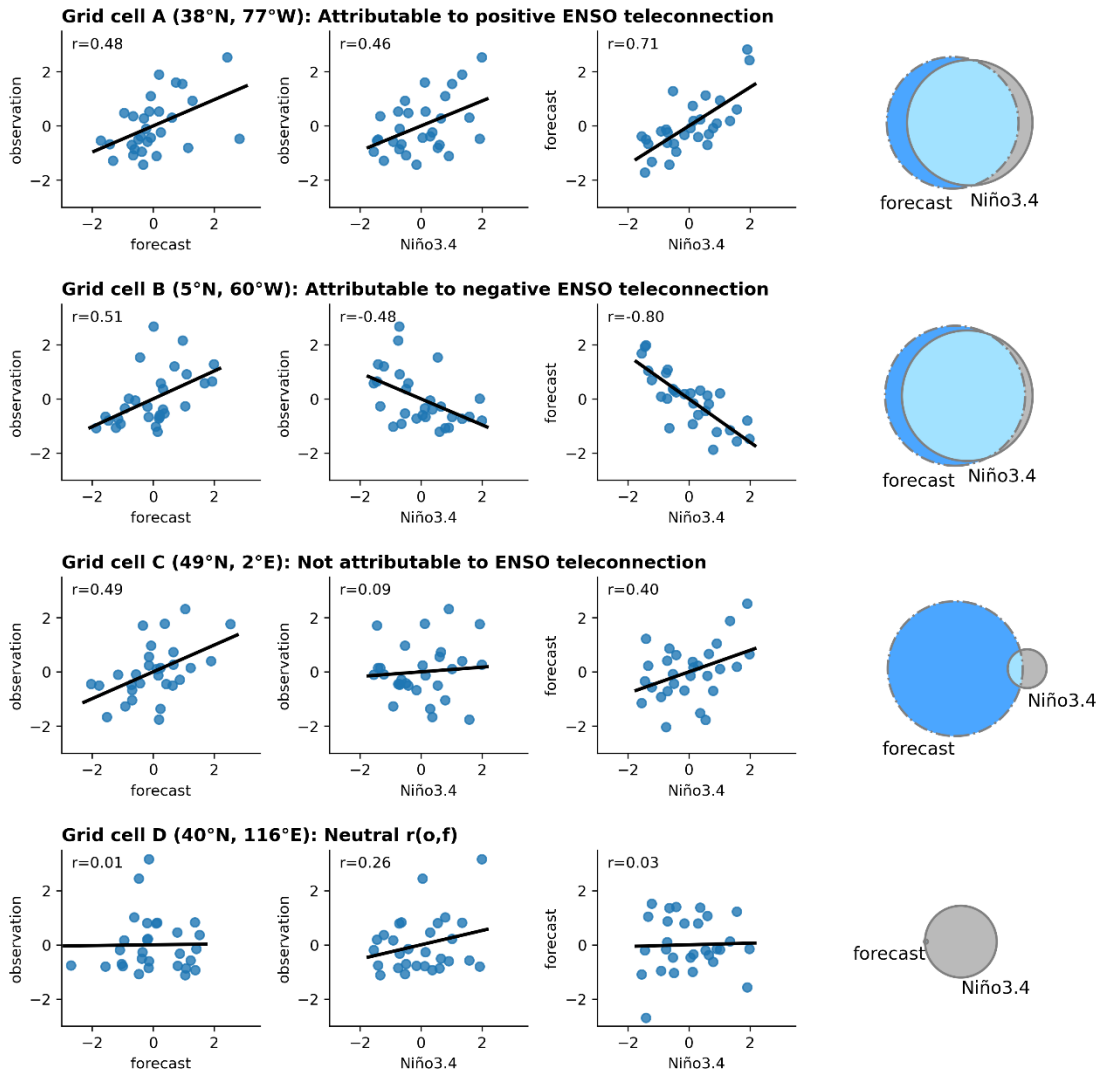
270   **Figure 8: Scatter plots of the relationships between normalized observation, forecast and Niño3.4 and Venn diagrams of the union and intersection operations for four selected grid cells.**

Grid cell A shown in the first row of Figure 8 presents the case of significantly positive anomaly correlation attributable to

positive ENSO teleconnection. The coordinate of the grid cell is (38°N, 77°W). In southern North America, DJF precipitation

275   is known to be modulated by the ENSO-induced Pacific North American (PNA) pattern (Jong et al., 2021). Specifically, in

southern North America, PNA tends to cause an enhanced DJF Pacific jet stream that extends further east than normal during El Niño events and there are nearly reversed patterns during La Niña events. Since the jet stream determines the paths of DJF storms, the PNA pattern enables ENSO to affect precipitation in southern North America. It can be seen that forecasts exhibit a high correlation with Niño3.4. This result suggests that CFSv2 forecasts can reasonably represent the influence of ENSO. As a result, R^2 explained by forecasts and Niño3.4 largely overlap in grid cell A.

Grid cell B shown in the second row of Figure 8 is for the case of significantly positive anomaly correlation attributable to negative ENSO teleconnection. Its coordinate is (5ºN, 60ºW). In DJF, there is a negative ENSO teleconnection over northern South America; it is owing to that ENSO-related SSTs drive changes in the climatological Walker circulation that promotes anomalous descending (ascending) motion and contributes to negative (positive) precipitation anomalies in El Niño (La Niña) events (Kayano & Andreoli, 2006). The high correlation between forecasts and Niño3.4 highlights the effectiveness of CFSv2 in capturing the negative ENSO teleconnection. There is a considerable intersection between the variability explained by forecasts and Niño3.4 in grid cell B. It is noted that some similarities in the Venn diagrams are observed for grid cells A and B at which ENSO teleconnection is respectively positive and negative. Specifically, $r(o$, Niño3.4$)$ is respectively 0.46 and – 0.48 at grid cells A and B. R^2 that is the focus of the Venn diagrams mathematically represents the squared value of correlation coefficient. Therefore, the similar Venn diagrams highlight that both positive and negative ENSO teleconnection can contribute to correlation skill.

Grid cell C displayed in the third row of Figure 8 is for the case of significantly positive correlation not attributable to ENSO teleconnection. Its coordinate is (49ºN, 2ºE). The remote influence of ENSO on Europe has pathways through the North Atlantic or Arctic regions, including the tropospheric and stratospheric bridges (Butler et al., 2014). However, the amplitude of ENSO impacts is weak and generally not significant in the European region (Butler et al., 2014). Besides, DJF precipitation in Europe is known to be modulated by the NAO (Greuell et al., 2018), the Eurasian snow cover extent and the Quasi-biennial Oscillation (Butler et al., 2014). It can be seen that while observed precipitation shows a neutral correlation with Niño3.4, CFSv2 forecasts explain a substantial fraction of observed precipitation variability. This result indicates the capability of CFSv2 in capturing teleconnection patterns other than ENSO.

Grid cell D shown in the last row of Figure 8 represents the case of neutral anomaly correlation. The coordinate is (40ºN, 116ºE). Over East Asia, precipitation is known to be influenced by the response of Rossby waves to ENSO (Yang et al., 2018). Also, winter monsoon activities in East Asia are profoundly influenced by wind-SST-evaporation feedbacks over tropical central Pacific to northwestern Pacific (Kim & Kug, 2018). It can be observed that there is a moderate but not significant correlation between observed precipitation and Niño3.4. However, CFSv2 forecasts exhibit a neutral anomaly correlation, suggesting that the information of ENSO teleconnection is not represented in the forecasts.

4.4 Extended analysis of the other seasons

The attribution analysis is further extended to the other seasons, i.e., MAM, JJA and SON. Global maps of the three cases of attribution are illustrated by season in Figure 9 and also in Figures S1 to S6 of the supplementary material. Overall, the results

of attribution vary considerably across the four seasons. It is generally owing to the facts that ENSO teleconnection varies by season (Kim & Kug, 2018; Steptoe et al., 2018; Wang et al., 2019) and that GCMs formulate not only ENSO but also other teleconnections (Saha et al., 2014; Jia et al., 2015; Delworth et al., 2020). Overall, the percentage of significantly positive anomaly correlation is 27.0%, 24.0% and 34.6% respectively in MAM, JJA and SON, which tend to be smaller than that in DJF. This result can be due to the seasonal cycle of ENSO, i.e., ENSO forcing tends to the strongest in DJF and it translates into weaker precipitation variability in the other seasons (Yang et al., 2018).

The percentage of significantly positive anomaly correlation attributable to positive ENSO teleconnection is respectively 7.1%, 6.3% and 7.0% in MAM, JJA and SON. Representative regions for this case are western United States in MAM (Pegion & Kumar, 2013), parts of South America in JJA (Cai et al., 2020) and Middle East in SON (Mariotti, 2007). 7.3%, 7.4% and 14.3% of grid cells are with significantly positive anomaly correlation attributable to negative ENSO teleconnection respectively in MAM, JJA and SON. One representative region is southeast Asia, where precipitation is strongly correlated with ENSO in MAM, JJA and SON (Jiang & Li, 2017); also, in Australia, precipitation in SON is found to be substantially influenced by the extratropical teleconnection pathway of ENSO (Cai & Weller, 2013). Furthermore, 12.6%, 10.3% and 13.3% of grid cells are with significantly positive anomaly correlation not attributable to ENSO teleconnection. This result calls for the investigation of other teleconnection patterns for GCM seasonal precipitation forecasts.
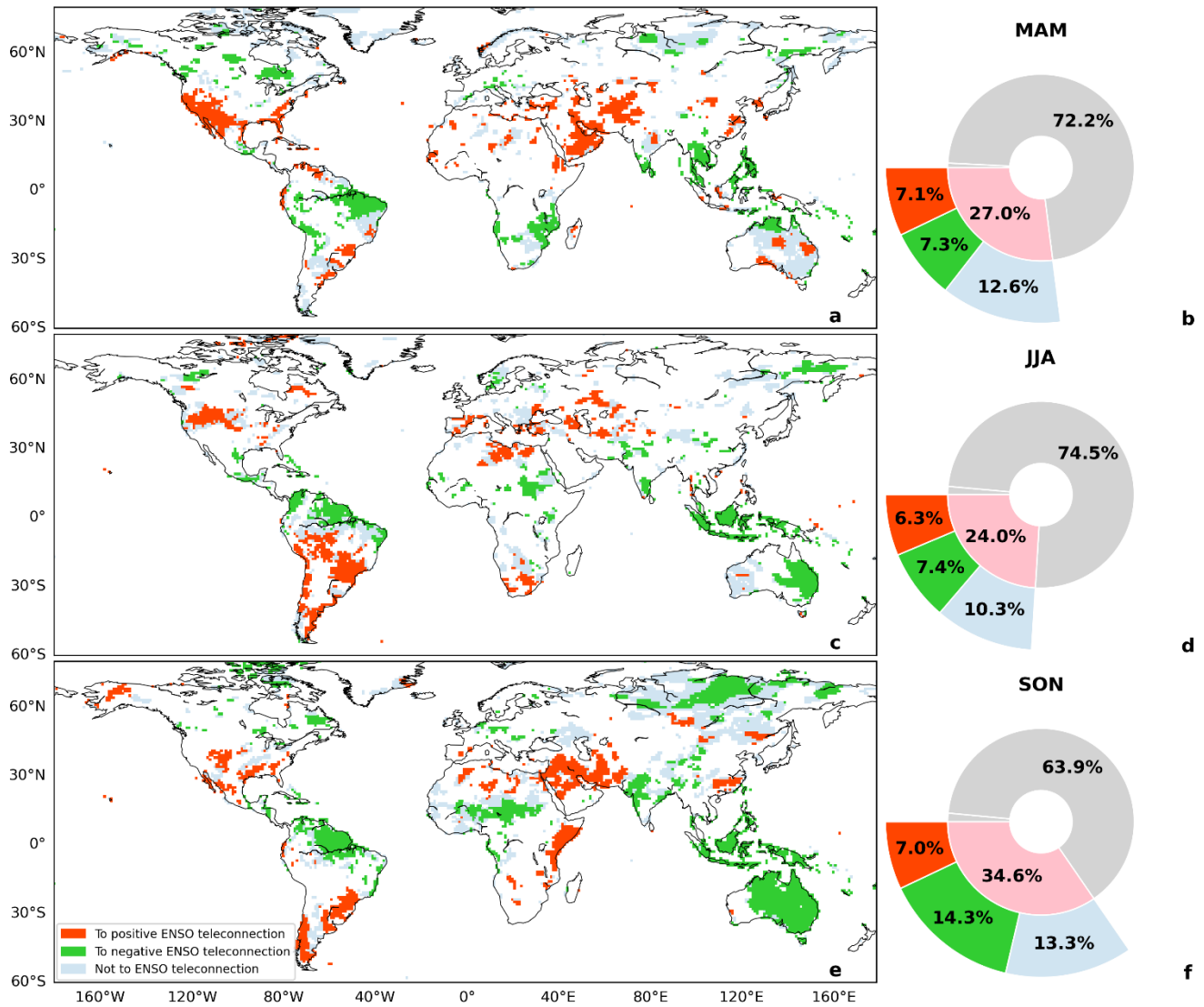
Figure 9: Spatial maps (left column) and sunburst diagrams (right column) of the three cases of attribution in MAM (upper part), JJA (middle part) and SON (lower part).

5 Discussion

330   The correlation skill between forecast and observed precipitation is one of the most important indicators of the usefulness of GCM forecasts (Yuan et al., 2011; Becker et al., 2014; Vano et al., 2014; Johnson et al., 2019; Zhao et al., 2020b). To facilitate forecast applications, correlation skill is conventionally calculated from data and then presented using spatial plotting (Zhao

et al., 2020a, 2020b). Focusing on the relationship between correlation skill and ENSO teleconnection, the present paper highlights that significantly positive anomaly correlation, which is always advantageous for practical applications of GCM forecasts (Vano et al., 2014; Yuan et al., 2015; Peng et al., 2018), can be attributed to positive (negative) ENSO teleconnection or not to ENSO. In DJF, significantly positive anomaly correlation for CFSv2 forecasts is attributable to positive ENSO teleconnection in southern North America and East Africa and it is attributable to negative ENSO teleconnection in northern South America and southern Africa. Moreover, significantly positive anomaly correlation in Europe can be attributable to teleconnections other than ENSO. The different cases of attribution also exist for MAM, JJA and SON, but their spatial extents vary considerably (Figures S2, S4 and S6 of the supplementary material). These results conform to previous findings that regions exhibiting positive (negative) ENSO teleconnection change substantially by season (Mason & Goddard, 2001; Chen & Kumar, 2020; Vashisht et al., 2021) and that performances of GCM forecasts vary by season (Vano et al., 2014; Johnson et al., 2019; Zhao et al., 2020b).

Lagged ENSO teleconnection and correlation skill by lead time are important issues for seasonal forecasting (Schepen et al., 2012; Peng et al., 2014; Steinschneider & Lall, 2016). A numerical experiment of attribution is performed for Niño3.4 indices at different time lags. Specifically, for precipitation in DJF, the concurrent Niño3.4 in the analysis is replaced by Niño3.4 in November, October and September so as to investigate the overlapping R^2 for 1-, 2- and 3-month lag ENSO teleconnection. Figures S7 to S10 in the supplementary material show that the results tend to be similar at the three lags; the similarities are generally owing to the temporal persistency of Niño3.4 (Yang et al., 2018). Furthermore, another experiment is devised for GCM forecasts at the lead time of 1, 2 and 3 months. That is, for precipitation in DJF, forecasts generated in November, October and September are used to replace forecasts generated in December in the analysis (Figures S11 to S14). It can be observed that the case of significantly positive anomaly correlation attributable to positive ENSO teleconnection remains for southern North America and that the case of significantly positive anomaly correlation attributable to negative ENSO teleconnection remains for northern South America and southern Africa.

The capability to formulate climate teleconnections is an essential part in the evaluation of GCM forecasts (Molod et al., 2020; Jong et al., 2021). Adding to previous studies that investigated GCM forecasts for regions subject to prominent ENSO influences (Pegion & Kumar, 2013; Manzanas et al., 2014; Jha et al., 2016), this paper presents an investigation of ENSO teleconnection at the global scale. For grid cells around the world, the ratio of significantly positive anomaly correlation attributable to positive (negative) ENSO teleconnection is respectively 10.8% (11.7%) in DJF, 7.1% (7.3%) in MAM, 6.3% (7.4%) in JJA and 7.0% (14.3%) in SON. Furthermore, the ratio of significantly positive anomaly correlation not attributable to ENSO teleconnection, which suggests that other climate teleconnections are at play in determining the skill of GCM forecasts, is respectively 16.9%, 12.6%, 10.3% and 13.3% in DJF, MAM, JJA and SON. Overall, the spatial plots and the attribution results can serve as a reference for further investigations of the effects of ENSO teleconnections and other climate patterns on the predictive performance of GCM forecasts.

6 Conclusions

Climate teleconnections, in particular ENSO, have been extensively used in conventional statistical hydrological forecasting. This paper is devoted to investigating the relationship between statistical ENSO teleconnection and correlation skill of dynamical CFSv2 forecasts. A novel mathematical approach is built upon the set theory by making use of the coefficient of determination (R^2) that measures the ratio of explained variance to total variance. Specifically, taking advantage of simple linear regression, the ratios of variance explained by GCM forecasts, Niño3.4 and their union are respectively obtained; then, the overlapping R^2 for GCM forecasts and Niño3.4 is derived based on the intersection operation. Based on the significance of overlapping R^2 and the sign of ENSO teleconnection, three cases of attribution are derived. They are significantly positive anomaly correlation attributable to positive ENSO teleconnection, attributable to negative ENSO teleconnection and not attributable to ENSO teleconnection. The effectiveness of the developed approach is demonstrated through the case study of CFSv2 seasonal forecasts of global precipitation. Spatial plots of the attribution are illustrated by season. The spatial patterns of forecast skill attributed to different types of ENSO teleconnections confirm previous studies associating seasonal precipitation variability with ENSO and highlight the capability of CFSv2 in capturing the pathways of ENSO teleconnections. The attribution method proposed in this paper can lay a basis for future evaluations of other teleconnections and investigations of predictability sources for GCM seasonal precipitation forecasts.

Acknowledgements

This study is jointly supported by the Ministry of Science and Technology of China (2017YFC1502600), the National Natural Science Foundation of China (51979295, 51861125203, 52109046 and U1911204) and the Guangdong Provincial Department of Science and Technology (2019ZT08G090).

Data Availability Statement

All data sets used in this study are publicly available. Both precipitation forecasts and the observations can be downloaded from the International Research Institute for Climate and Society, Earth Institute, Columbia University (https://iridl.ldeo.columbia.edu/SOURCES/.Models/.NMME/). The Niño3.4 index is download from the NOAA Physical Sciences Laboratory (https://psl.noaa.gov/data/climateindices/list/).

References

Beck, H. E., Pan, M., Roy, T., Weedon, G. P., Pappenberger, F., van Dijk, A. I. J. M., et al. (2019). Daily evaluation of 26 precipitation datasets using Stage-IV gauge-radar data for the CONUS. *Hydrology and Earth System Sciences, 23*(1), 207-224. https://doi.org/10.5194/hess-23-207-2019

Becker, E., Kirtman, Ben P., & Pegion, K. (2020). Evolution of the North American Multi‑Model Ensemble. *Geophysical Research Letters, 47*(9). https://doi.org/10.1029/2020GL087408

395 Butler, A. H., Polvani, L. M., & Deser, C. (2014). Separating the stratospheric and tropospheric pathways of El Niño–Southern Oscillation teleconnections. *Environmental Research Letters, 9*(2). https://doi.org/10.1088/1748-9326/9/2/024014

Cai, W., McPhaden, M. J., Grimm, A. M., Rodrigues, R. R., Taschetto, A. S., Garreaud, R. D., et al. (2020). Climate impacts of the El Niño–Southern Oscillation on South America. *Nature Reviews Earth & Environment, 1*(4), 215-231. https://doi.org/10.1038/s43017-020-0040-3

Cai, W., Sullivan, A., & Cowan, T. (2009). Rainfall Teleconnections with Indo-Pacific Variability in the WCRP CMIP3 Models. *Journal of Climate, 22*(19), 5046-5071. https://doi.org/10.1175/2009JCLI2694.1

Cai, W., & Weller, E. (2013). Asymmetry in the IOD and ENSO Teleconnection in a CMIP5 Model Ensemble and Its Relevance to Regional Rainfall. *Journal of Climate, 26*(14), 5139-5149. https://doi.org/10.1175/JCLI-D-12-00789.1

Chen, M., & Kumar, A. (2016). The utility of seasonal hindcast database for the analysis of climate variability: an example. *Climate Dynamics, 48*(1-2), 265-279. https://doi.org/10.1007/s00382-016-3073-z

410 Chen, M., & Kumar, A. (2020). Understanding Skill of Seasonal Mean Precipitation Prediction over California during Boreal Winter and Role of Predictability Limits. *Journal of Climate, 33*(14), 6141-6163. https://doi.org/10.1175/jcli-d-19-0275.1

Delworth, T. L., Cooke, W. F., Adcroft, A., Bushuk, M., Chen, J. H., Dunne, K. A., et al. (2020). SPEAR: The Next Generation GFDL Modeling System for Seasonal to Multidecadal Prediction and Projection. *Journal of Advances in Modeling Earth Systems, 12*(3). https://doi.org/10.1029/2019ms001895

Demargne, J., Wu, L., Regonda, S. K., Brown, J. D., Lee, H., He, M., et al. (2014). The Science of NOAA's Operational Hydrologic Ensemble Forecast Service. *Bulletin of the American Meteorological Society, 95*(1), 79-98. https://doi.org/10.1175/BAMS-D-12-00081.1

420 Doblas-Reyes, F. J., García-Serrano, J., Lienert, F., Biescas, A. P., & Rodrigues, L. R. L. (2013). Seasonal climate predictability and forecasting: status and prospects. *Wiley Interdisciplinary Reviews: Climate Change, 4*(4), 245-268. https://doi.org/10.1002/wcc.217

Feng, S., & Hao, Z. (2021). Quantitative contribution of ENSO to precipitation-temperature dependence and associated compound dry and hot events. *Atmospheric Research, 260.* https://doi.org/10.1016/j.atmosres.2021.105695

Fu, R., Dickinson, R. E., & Newkirk, B. (1997). Response of the upper tropospheric humidity and moisture transport to changes of tropical convection. A comparison between observations and a GCM over an ENSO cycle. *Geophysical Research Letters, 24*(19), 2371-2374. https://doi.org/10.1029/97GL02505

430 Gong, H., Wang, L., Chen, W., Nath, D., Huang, G., & Tao, W. (2015). Diverse Influences of ENSO on the East Asian–Western Pacific Winter Climate Tied to Different ENSO Properties in CMIP5 Models. *Journal of Climate, 28*(6), 2187-2202. https://doi.org/10.1175/JCLI-D-14-00405.1

Greuell, W., Franssen, W. H. P., Biemans, H., & Hutjes, R. W. A. (2018). Seasonal streamflow forecasts for Europe – Part I: Hindcast verification with pseudo- and real observations. *Hydrology and Earth*
435 *System Sciences, 22*(6), 3453-3472. https://doi.org/10.5194/hess-22-3453-2018

Howard, E., Washington, R., & Hodges, K. I. (2019). Tropical Lows in Southern Africa: Tracks, Rainfall Contributions, and the Role of ENSO. *Journal of Geophysical Research: Atmospheres, 124*(21), 11009-11032. https://doi.org/10.1029/2019jd030803

Huffman, G. J., Bolvin, D. T., Nelkin, E. J., Wolff, D. B., Adler, R. F., Gu, G., et al. (2007). The TRMM
440 Multisatellite Precipitation Analysis (TMPA): Quasi-Global, Multiyear, Combined-Sensor Precipitation Estimates at Fine Scales %J Journal of Hydrometeorology. *Journal of Hydrometeorology, 8*(1), 38-55. https://doi.org/10.1175/jhm560.1

Infanti, J. M., & Kirtman, B. P. (2015). North American rainfall and temperature prediction response to the diversity of ENSO. *Climate Dynamics, 46*(9-10), 3007-3023. https://doi.org/10.1007/s00382-
445 015-2749-0

Jha, B., Kumar, A., & Hu, Z.-Z. (2016). An update on the estimate of predictability of seasonal mean atmospheric variability using North American Multi-Model Ensemble. *Climate Dynamics.* https://doi.org/10.1007/s00382-016-3217-1

Jia, L., Yang, X., Vecchi, G. A., Gudgel, R. G., Delworth, T. L., Rosati, A., et al. (2015). Improved
450 Seasonal Prediction of Temperature and Precipitation over Land in a High-Resolution GFDL Climate Model. *Journal of Climate, 28*(5), 2044-2062. https://doi.org/10.1175/jcli-d-14-00112.1

Jiang, L., & Li, T. (2017). Why rainfall response to El Niño over Maritime Continent is weaker and non-uniform in boreal winter than in boreal summer. *Climate Dynamics, 51*(4), 1465-1483. https://doi.org/10.1007/s00382-017-3965-6

455 Johnson, S. J., Stockdale, T. N., Ferranti, L., Balmaseda, M. A., Molteni, F., Magnusson, L., et al. (2019). SEAS5: the new ECMWF seasonal forecast system. *Geosci. Model Dev., 12*(3), 1087-1117. https://doi.org/10.5194/gmd-12-1087-2019

Jong, B.-T., Ting, M., & Seager, R. (2021). Assessing ENSO Summer Teleconnections, Impacts, and Predictability in North America. *Journal of Climate, 34*(9), 3629-3643.
460 https://doi.org/10.1175/jcli-d-20-0761.1

Kayano, M. T., & Andreoli, R. V. (2006). Relationships between rainfall anomalies over northeastern Brazil and the El Niño–Southern Oscillation. *Journal of Geophysical Research, 111*(D13). https://doi.org/10.1029/2005JD006142

Kim, H.-M., Webster, P. J., & Curry, J. A. (2012). Seasonal prediction skill of ECMWF System 4 and
465 NCEP CFSv2 retrospective forecast for the Northern Hemisphere Winter. *Climate Dynamics, 39*(12), 2957-2973. https://doi.org/10.1007/s00382-012-1364-6

Kim, S., & Kug, J. S. (2018). What Controls ENSO Teleconnection to East Asia? Role of Western North Pacific Precipitation in ENSO Teleconnection to East Asia. *Journal of Geophysical Research: Atmospheres, 123*(18). https://doi.org/10.1029/2018JD028935

470 Kim, S., Son, H.-Y., & Kug, J.-S. (2016). How well do climate models simulate atmospheric teleconnctions over the North Pacific and East Asia associated with ENSO? *Climate Dynamics, 48*(3-4), 971-985. https://doi.org/10.1007/s00382-016-3121-8

Kirtman, B. P., Min, D., Infanti, J. M., Kinter, J. L., Paolino, D. A., Zhang, Q., et al. (2014). The North American Multimodel Ensemble: Phase-1 Seasonal-to-Interannual Prediction; Phase-2 toward 475 Developing Intraseasonal Prediction. *Bulletin of the American Meteorological Society, 95*(4), 585-601. https://doi.org/10.1175/BAMS-D-12-00050.1

Koster, R. D., Mahanama, S. P. P., Yamada, T. J., Balsamo, G., Berg, A. A., Boisserie, M., et al. (2010). Contribution of land surface initialization to subseasonal forecast skill: First results from a multi-model experiment. *Geophysical Research Letters, 37*(2). https://doi.org/10.1029/2009GL041677

480 Krause, P., Boyle, D. P., & Bäse, F. (2005). Comparison of different efficiency criteria for hydrological model assessment. *Adv. Geosci., 5*, 89-97. https://doi.org/10.5194/adgeo-5-89-2005

Lakshmi, D. D., & Satyanarayana, A. N. V. (2019). Influence of atmospheric rivers in the occurrence of devastating flood associated with extreme precipitation events over Chennai using different reanalysis data sets. *Atmospheric Research, 215*, 12-36. 485 https://doi.org/10.1016/j.atmosres.2018.08.016

Lima, C. H. R., & Lall, U. (2010). Climate informed monthly streamflow forecasts for the Brazilian hydropower network using a periodic ridge regression model. *Journal of Hydrology, 380*(3-4), 438-449. https://doi.org/10.1016/j.jhydrol.2009.11.016

Manzanas, R., Frías, M. D., Cofiño, A. S., & Gutiérrez, J. M. (2014). Validation of 40 year multimodel 490 seasonal precipitation forecasts: The role of ENSO on the global skill. *Journal of Geophysical Research: Atmospheres, 119*(4), 1708-1719. https://doi.org/10.1002/2013JD020680

Mariotti, A. (2007). How ENSO impacts precipitation in southwest central Asia. *Geophysical Research Letters, 34*(16). https://doi.org/10.1029/2007GL030078

Mason, S. J., & Goddard, L. (2001). Probabilistic precipitation anomalies associated with ENSO. *Bulletin* 495 *of the American Meteorological Society, 82*(4), 619-638. https://doi.org/10.1175/1520-0477(2001)082<0619:PPAAWE>2.3.CO;2

Mendoza, P. A., Wood, A. W., Clark, E., Rothwell, E., Clark, M. P., Nijssen, B., et al. (2017). An intercomparison of approaches for improving operational seasonal streamflow forecasts. *Hydrology and Earth System Sciences, 21*(7), 3915-3935. https://doi.org/10.5194/hess-21-3915-500 2017

Merryfield, W. J., Lee, W.-S., Boer, G. J., Kharin, V. V., Scinocca, J. F., Flato, G. M., et al. (2013). The Canadian Seasonal to Interannual Prediction System. Part I: Models and Initialization. *Monthly Weather Review, 141*(8), 2910-2945. https://doi.org/10.1175/mwr-d-12-00216.1

Minami, A., & Takaya, Y. (2020). Enhanced Northern Hemisphere Correlation Skill of Subseasonal Predictions in the Strong Negative Phase of the Arctic Oscillation. *Journal of Geophysical Research: Atmospheres, 125*(10). https://doi.org/10.1029/2019JD031268

Molod, A., Hackert, E., Vikhliaev, Y., Zhao, B., Barahona, D., Vernieres, G., et al. (2020). GEOS‐S2S Version 2: The GMAO High‐Resolution Coupled Model and Assimilation System for Seasonal Prediction. *Journal of Geophysical Research: Atmospheres, 125*(5). https://doi.org/10.1029/2019JD031767

Molteni, F., Stockdale, T., Balmaseda, M., Balsamo, G., Buizza, R., Ferranti, L., et al. (2011). *The new ECMWF seasonal forecast system (System 4)* (Vol. 49): European Centre for Medium-Range Weather Forecasts Reading.

Mortensen, E., Wu, S., Notaro, M., Vavrus, S., Montgomery, R., De Piérola, J., et al. (2018). Regression-based season-ahead drought prediction for southern Peru conditioned on large-scale climate variables. *Hydrology and Earth System Sciences, 22*(1), 287-303. https://doi.org/10.5194/hess-22-287-2018

Neelin, J. D., & Langenbrunner, B. (2013). Analyzing ENSO Teleconnections in CMIP Models as a Measure of Model Fidelity in Simulating Precipitation. *Journal of Climate, 26*(13), 4431-4446. https://doi.org/10.1175/jcli-d-12-00542.1

Pegion, K., & Kumar, A. (2013). Does An ENSO-Conditional Skill Mask Improve Seasonal Predictions? *Monthly Weather Review, 141*(12), 4515-4533. https://doi.org/10.1175/mwr-d-12-00317.1

Peng, B., Guan, K., Pan, M., & Li, Y. (2018). Benefits of Seasonal Climate Prediction and Satellite Data for Forecasting U.S. Maize Yield. *Geophysical Research Letters, 45*(18), 9662-9671. https://doi.org/10.1029/2018gl079291

Peng, Z., Wang, Q. J., Bennett, J. C., Pokhrel, P., & Wang, Z. (2014). Seasonal precipitation forecasts over China using monthly large-scale oceanic-atmospheric indices. *Journal of Hydrology, 519*, 792-802. https://doi.org/10.1016/j.jhydrol.2014.08.012

Quan, X., Hoerling, M., Whitaker, J., Bates, G., & Xu, T. (2006). Diagnosing Sources of U.S. Seasonal Forecast Skill. *Journal of Climate, 19*(13), 3279-3293. https://doi.org/10.1175/JCLI3789.1

Rivera, J. A., & Arnould, G. (2020). Evaluation of the ability of CMIP6 models to simulate precipitation over Southwestern South America: Climatic features and long-term trends (1901–2014). *Atmospheric Research, 241*, 104953. https://doi.org/10.1016/j.atmosres.2020.104953

Robertson, D. E., Shrestha, D. L., & Wang, Q. J. (2013). Post-processing rainfall forecasts from numerical weather prediction models for short-term streamflow forecasting. *Hydrology and Earth System Sciences, 17*(9), 3587-3603. https://doi.org/10.5194/hess-17-3587-2013

Saha, S., Moorthi, S., Pan, H.-L., Wu, X., Wang, J., Nadiga, S., et al. (2010). The NCEP Climate Forecast System Reanalysis. *Bulletin of the American Meteorological Society, 91*(8), 1015-1058. https://doi.org/10.1175/2010bams3001.1

540   Saha, S., Moorthi, S., Wu, X., Wang, J., Nadiga, S., Tripp, P., et al. (2014). The NCEP Climate Forecast System Version 2. *Journal of Climate, 27*(6), 2185-2208. https://doi.org/10.1175/jcli-d-12-00823.1

Schepen, A., Everingham, Y., & Wang, Q. J. (2020). On the Joint Calibration of Multivariate Seasonal Climate Forecasts from GCMs. *Monthly Weather Review, 148*(1), 437-456.
545   https://doi.org/10.1175/mwr-d-19-0046.1

Schepen, A., Wang, Q. J., & Robertson, D. (2012). Evidence for Using Lagged Climate Indices to Forecast Australian Seasonal Rainfall. *Journal of Climate, 25*(4), 1230-1246. https://doi.org/10.1175/jcli-d-11-00156.1

Schneider, U., Ziese, M., Meyer-Christoffer, A., Finger, P., Rustemeier, E., & Becker, A. (2016). The new
550   portfolio of global precipitation data products of the Global Precipitation Climatology Centre suitable to assess and quantify the global water cycle and resources. *Proceedings of the International Association of Hydrological Sciences, 374*, 29-34. https://doi.org/10.5194/piahs-374-29-2016

Scofield, R. A., & Kuligowski, R. J. (2003). Status and Outlook of Operational Satellite Precipitation
555   Algorithms for Extreme-Precipitation Events. *Weather and Forecasting, 18*(6), 1037-1051. https://doi.org/10.1175/1520-0434(2003)018<1037:Saooos>2.0.Co;2

Shin, C.-S., Huang, B., & Kumar, A. (2019). Predictive Skill and Predictable Patterns of the U.S. Seasonal Precipitation in CFSv2 Reforecasts of 60 Years (1958–2017). *Journal of Climate, 32*(24), 8603-8637. https://doi.org/10.1175/jcli-d-19-0230.1

560   Steinschneider, S., & Lall, U. (2016). El Niño and the U.S. precipitation and floods: What was expected for the January-March 2016 winter hydroclimate that is now unfolding? *Water Resources Research, 52*(2), 1498-1501. https://doi.org/10.1002/2015WR018470

Steptoe, H., Jones, S. E. O., & Fox, H. (2018). Correlations Between Extreme Atmospheric Hazards and Global Teleconnections: Implications for Multihazard Resilience. *Reviews of Geophysics, 56*(1),
565   50-78. https://doi.org/10.1002/2017rg000567

Strazzo, S., Collins, D. C., Schepen, A., Wang, Q. J., Becker, E., & Jia, L. (2019). Application of a Hybrid Statistical–Dynamical System to Seasonal Prediction of North American Temperature and Precipitation. *Monthly Weather Review, 147*(2), 607-625. https://doi.org/10.1175/mwr-d-18-0156.1

570   Tesfa, T. K., Leung, L. R., & Ghan, S. J. (2020). Exploring Topography-Based Methods for Downscaling Subgrid Precipitation for Use in Earth System Models. *Journal of Geophysical Research: Atmospheres, 125*(5), e2019JD031456. https://doi.org/10.1029/2019JD031456

Ushio, T., Sasashige, K., Kubota, T., Shige, S., Okamoto, K. i., Aonashi, K., et al. (2009). A Kalman Filter Approach to the Global Satellite Mapping of Precipitation (GSMaP) from Combined Passive
575   Microwave and Infrared Radiometric Data. *Journal of the Meteorological Society of Japan, 87A*, 137-151. https://doi.org/10.2151/jmsj.87A.137

Vano, J. A., Udall, B., Cayan, D. R., Overpeck, J. T., Brekke, L. D., Das, T., et al. (2014). Understanding Uncertainties in Future Colorado River Streamflow. *Bulletin of the American Meteorological Society, 95*(1), 59-78. https://doi.org/10.1175/bams-d-12-00228.1

Vashisht, A., Zaitchik, B., & Gnanadesikan, A. (2021). ENSO Teleconnection to Eastern African Summer Rainfall in Global Climate Models: Role of the Tropical Easterly Jet. *Journal of Climate, 34*(1), 293-312. https://doi.org/10.1175/jcli-d-20-0222.1

Wang, H.-M., Chen, J., Xu, C.-Y., Chen, H., Guo, S., Xie, P., & Li, X. (2019). Does the weighting of climate simulations result in a better quantification of hydrological impacts? *Hydrology and Earth System Sciences, 23*(10), 4033-4050. https://doi.org/10.5194/hess-23-4033-2019

Wang, J., Wang, X., Lei, X. h., Wang, H., Zhang, X. h., You, J. j., et al. (2020). Teleconnection analysis of monthly streamflow using ensemble empirical mode decomposition. *Journal of Hydrology, 582*. https://doi.org/10.1016/j.jhydrol.2019.124411

Wang, P.-H., Minnis, P., Wielicki, B. A., Wong, T., Cess, R. D., Zhang, M., et al. (2003). Characteristics of the 1997/1998 El Niño cloud distributions from SAGE II observations. *Journal of Geophysical Research: Atmospheres, 108*(D1), AAC 5-1-AAC 5-11. https://doi.org/10.1029/2002JD002501

Wu, H., Adler, R. F., Tian, Y., Huffman, G. J., Li, H., & Wang, J. (2014). Real-time global flood estimation using satellite-based precipitation and a coupled land surface and routing model. *Water Resources Research, 50*(3), 2693-2717. https://doi.org/10.1002/2013wr014710

Xie, P., Arkin, P., & Janowiak, J. (2007). CMAP: The CPC merged analysis of precipitation. In (Vol. 28, pp. 319-328).

Xie, P., Chen, M., & Shi, W. (2010). *CPC unified gauge-based analysis of global daily precipitation.* Paper presented at the Preprints, 24th Conf. on Hydrology, Atlanta, GA, Amer. Meteor. Soc.

Yang, S., & Jiang, X. (2014). Prediction of Eastern and Central Pacific ENSO Events and Their Impacts on East Asian Climate by the NCEP Climate Forecast System. *Journal of Climate, 27*(12), 4451-4472. https://doi.org/10.1175/JCLI-D-13-00471.1

Yang, S., Li, Z., Yu, J.-Y., Hu, X., Dong, W., & He, S. (2018). El Niño–Southern Oscillation and its impact in the changing climate. *National Science Review, 5*(6), 840-857. https://doi.org/10.1093/nsr/nwy046

Yuan, X., Wood, E. F., & Liang, M. (2014). Integrating weather and climate prediction: Toward seamless hydrologic forecasting. *Geophysical Research Letters, 41*(16), 5891-5896. https://doi.org/10.1002/2014gl061076

Yuan, X., Wood, E. F., Luo, L., & Pan, M. (2011). A first look at Climate Forecast System version 2 (CFSv2) for hydrological seasonal prediction. *Geophysical Research Letters, 38*(13). https://doi.org/10.1029/2011GL047792

Zhao, T., Chen, H., Xu, W., Cai, H., Yan, D., & Chen, X. (2020a). Spatial association of anomaly correlation for GCM seasonal forecasts of global precipitation. *Climate Dynamics*. https://doi.org/10.1007/s00382-020-05384-2

Zhao, T., Zhang, W., Zhang, Y., Liu, Z., & Chen, X. (2020b). Significant spatial patterns from the GCM seasonal forecasts of global precipitation. *Hydrology and Earth System Sciences, 24*(1), 1-16. https://doi.org/10.5194/hess-24-1-2020

Zhao, T., Zhang, Y., & Chen, X. (2019). Predictive performance of NMME seasonal forecasts of global precipitation: A spatial-temporal perspective. *Journal of Hydrology, 570*, 17-25. https://doi.org/10.1016/j.jhydrol.2018.12.036